THE ASTROPHYSICAL JOURNAL, 527:662–672, 1999 December 20

THE EVOLUTION OF THE GALAXY SIZES IN THE NEW TECHNOLOGY TELESCOPE DEEP FIELD: A COMPARISON WITH COLD DARK MATTER MODELS

F. POLI,[1] E. GIALLONGO,[1] N. MENCI,[1] S. D'ODORICO,[2] AND A. FONTANA[1]
Received 1999 April 21; accepted 1999 July 30

ABSTRACT

The sizes of the field galaxies with $I \leq 25$ have been measured in the New Technology Telescope (NTT) Deep Field. Intrinsic sizes have been obtained after deconvolution of the point-spread function with a multi-Gaussian method. The reliability of the method has been tested using both simulated data and *Hubble Space Telescope* (*HST*) observations of the same field. The distribution of the half-light radii is peaked at $r_{\rm hl} \simeq 0''.3$, in good agreement with that derived from *HST* images at the same magnitude. An approximate morphological classification has been obtained using the asymmetry and concentration parameters. The intrinsic sizes of the galaxies are shown as a function of their redshifts and absolute magnitudes using photometric redshifts derived from the multicolor catalog. While the brighter galaxies with morphological parameters typical of the normal spirals show a flat distribution in the range $r_d = 1 - 6$ kpc, the fainter population at $0.4 < z < 0.8$ dominates at small sizes. To explore the significance of this behavior, an analytical rendition of the standard cold dark matter model for the disk size evolution has been computed. The model showing the best fit to the local luminosity function and the Tully-Fisher relation is able to reproduce at intermediate redshifts a size distribution in general agreement with the observations, although it tends to underestimate the number of galaxies fainter than $M_B \sim -19$ with disk sizes $r_d \sim 1$–2 kpc.

Subject headings: galaxies: evolution — galaxies: formation — galaxies: fundamental parameters

1. INTRODUCTION

Deep multicolor surveys from *Hubble Space Telescope* (*HST*) and ground-based telescopes coupled with deep spectroscopy on 10 m class telescopes (Keck, Very Large Telescope) are leading to remarkable progress in our understanding of the galaxy formation and evolution. In particular, there has been great improvement in the knowledge of the epoch of star formation. The first determinations of the global star formation history suggested a peak at $z \approx 1.5$ with a further decline from $z \simeq 2$ to $z \approx 4$ (Madau et al. 1996; Connolly et al. 1997). In this scenario, more than 80% of the stars would have been formed recently at $z < 2$.

Such a picture would be in rough agreement with the cold dark matter (CDM) models of galaxy formation, which predict the star formation to be a gradual process governed by gas cooling and supernovae feedback. The timescale of the process is strongly related to the rate at which the mass is hierarchically assembled to form larger galaxies from smaller structures (White & Frenk 1991; Cole et al. 1994; Kauffmann, White & Guiderdoni 1993; Baugh et al. 1998).

However, the above scenario is presently challenged by recent indications that the observed decline at $z > 2$ is affected by incompleteness in the color selection and by dust extinction. In fact, more recent observational evidence limited to the optically selected galaxies points toward a flat star formation rate (SFR) for $z > 2$ (Giallongo et al. 1998; Pascarelle, Lanzetta, & Fernandez-Soto 1998; Steidel et al. 1999).

A more precise test of the galaxy formation scenarios involves the study of the size and morphological distribution of galaxies with cosmic time, since this is related to the main feature of the hierarchical models, namely, the growth of mass and sizes of typical condensations. Indeed, although the global star formation history is a crucial issue in galaxy formation, it is an integrated quantity; even a flat SFR could be consistent with the CDM picture by tuning the parameters describing the gas cooling and the supernovae feedback in galaxies.

The first observational investigations of the *differential* evolution of the galaxy population over the redshift range $0 < z < 1$ were carried out by Lilly et al. (1995), Cowie et al. (1996), and Ellis et al. (1996) by means of spectroscopic redshift surveys. The observed decrease with the cosmic time of the blue star-forming galaxy population showing strong emission lines has been further investigated using *HST*. The decline is a mixture of stellar evolution in normal spirals and strong evolution in low-luminosity irregulars (Schade et al. 1995; Brinchmann et al. 1998; Lilly et al. 1998) whose local counterparts now comprise the faint end of the local luminosity function (Zucca et al. 1997).

Subsequently, the study of the Hubble Deep Field (HDF) (Williams et al. 1996) has resulted in a strong improvement in the knowledge of the galaxy morphology at high redshift (Abraham et al. 1996; Odewahn et al. 1996; Driver et al. 1998) showing a high fraction of faint irregular galaxies. Most of these galaxies have small sizes resulting in a physical extent of the order of 3–5 kpc at $z \sim 1$ (Glazebrook et al. 1998). Such small sizes, if compared with the present-day galaxy morphology included in the Hubble sequence, could imply physical growth and merging occurring with increasing cosmic time (Bouwens, Broadhurst, & Silk 1997), in qualitative agreement with the hierarchical clustering picture. On the other hand, the indications for a slow evolution of the spiral population constituted by the presence of large, relatively bright spirals at $z \sim 0.6$ (Schade et al. 1995) are difficult to fit into the picture of the CDM-like models. Indeed, the dissipative formation of galactic disks in CDM halos predicted by the hierarchical clustering scenario produces spirals whose size strongly decreases as the formation

[1] Osservatorio Astronomico di Roma, via dell'Osservatorio, I-00040 Monteporzio, Italy.

[2] European Southern Observatory, Karl Schwarzschild Strasse 2, D-85748 Garching, Germany.

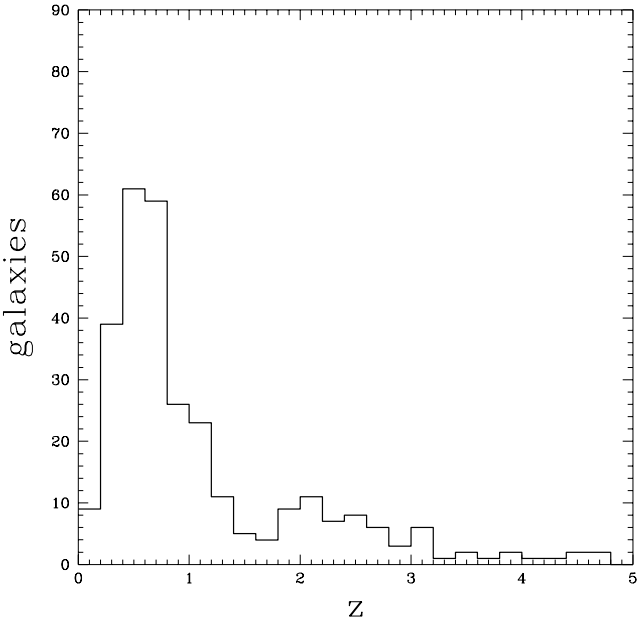

FIG. 1.—Photometric redshift distribution of galaxies with $I \leq 25$ in the NDF.

redshift increases. For this reason, gas cooling in the CDM halos has to be delayed to low redshifts ($z < 1$). The comparison becomes more stringent for the lower luminosity spirals where the predicted sizes are very small at high redshifts.

A wide-field survey of faint galaxies observed with *HST* would be the ideal sample to clarify the issue and to provide a differential and quantitative test to CDM galaxy formation theories. However, deep photometry from *HST* can be obtained only on small areas. On the contrary, wide-field surveys of faint galaxies can be obtained using ground-based instrumentation but at lower resolution (FWHM $\sim$ 0.″5–1″).

In this paper we have exploited the deep photometric information of the New Technology Telescope (NTT) Deep Field (Arnouts et al. 1999) obtained under condition of subarcsecond seeing at the ESO NTT to derive morphological information after appropriate seeing deconvolution (§ 2). The reliability of the deconvolution technique has been tested by means of numerical simulations and particularly by checking on somewhat shallower *HST* images of the same galaxy field retrieved from the *HST* archive. The results show that it is possible to derive the radial intensity profiles of galaxies with $I \leq 25$ from ground-based imaging with FWHM $< 1''$ (§ 3).

The derived intrinsic angular sizes are then converted into physical sizes adopting reliable photometric redshifts estimated from the *UBVRIJK* multicolor distribution of each galaxy in the catalog. The galaxy morphological distribution in redshift and luminosity is shown in § 4 and is compared with that predicted by hierarchical clustering models for the disk formation in § 5. The conclusions are presented in § 6.

2. THE GALAXY CATALOG

The galaxy catalog has been obtained from the NTT Deep Field (NDF) (Arnouts et al. 1999). The optical observations were obtained in the Johnson *BV* and Gunn *R,I* broadband filters with the $1k \times 1k$ SUSI camera on the ESO NTT. The resulting field of view is ~ 5 arcmin^2.

The 3 σ magnitude limits are $B = 27.5$, $V = 27$, $R = 26.5$, and $I = 26.5$, and the average seeing was $\sim$0.″8 (see Arnouts et al. 1999 for further details).

Deep ultraviolet images have been added with the SUSI-2 camera at the NTT reaching a 3 σ upper limit of $U = 26$. Also deep near-infrared observations have been added with the SOFI instrument at the NTT reaching 3 σ magnitude limits of $J \sim 23.5$ and $K' \sim 21.7$.

The galaxy catalog has been extracted from the sum of the *BVRI* weighted frames to detect objects at very faint level in the four bands (Arnouts et al. 1999). The object detection and photometry have been performed with the Sextractor image analysis package (Bertin & Arnouts 1996). Total magnitudes in the *UBVRIJK* bands were computed from isophotal magnitudes for galaxies brighter than $I = 23.25$ and from aperture magnitudes in 2.″2 corrected to 5″ for fainter objects. Colors are computed in a 2″ diameter aperture in the same sky area in all the bands after correction for the different seeing conditions. Details on the data reduction and photometry are fully discussed in Fontana et al. (1999).

To each galaxy in the *UBVRIJK* catalog, a photometric redshift estimate has been assigned with the same best fitting procedure applied in the contiguous BR 1202−0725 field (Giallongo et al. 1998). This has been obtained through a comparison of the observed colors with those predicted by spectral synthesis (GISSEL) models (Bruzual & Charlot 1993) including UV absorption by the intergalactic medium and dust reddening. The catalog of the photometric redshifts is presented in Fontana et al. (1999). The resulting typical redshift accuracy is $\Delta z \sim 0.1$ up to $z \sim 1.5$ and $\Delta z \sim 0.15$ at larger redshifts.

The redshift distribution in the NTT Deep Field is shown in Figure 1 for galaxies with $I \leq 25$. As derived in other fields of similar depth, the bulk of the galaxies present are at intermediate redshifts $z \sim 0.5$–0.8 with a tail in the distribution up to $z \sim 4$.

The shape of the optical counts in this field suggests negligible correction for incompleteness at $I = 25$ (Arnouts et al. 1999); thus, the morphological study described in the next sections should be considered complete to this magnitude limit.

3. THE RADIAL INTENSITY PROFILES OF FAINT GALAXIES

The estimate of the intrinsic radial intensity profiles derived from deep ground-based images of faint galaxies is a complex task. Indeed, *HST* images of galaxies with $I \sim 25$ have shown that most of them have typical sizes corresponding to half-light radii $r_{hl} \sim 0.''3$, which are smaller than the typical HWHM $\sim 0.''5$ present in ground-based deep images.

Accurate and reliable deconvolution techniques must be applied to obtain any statistical information about the intrinsic half-light radii of faint galaxies observed from the ground. Any deconvolution technique depends of course on the accurate knowledge of the instrumental profile (PSF) and on the intrinsic shape assumed for the galaxies. An accurate reconstruction of the instrumental profile is generally done through an average of the stellar profiles with high signal-to-noise ratio in images with good oversampling.

Concerning the intrinsic shape of the galaxies, instead of assuming a specified profile, we adopted the multi-Gaussian

deconvolution analysis studied in detail by Bendinelli (1991) and also recently applied to faint elliptical galaxies in the Hubble Deep Field (HDF) by Fasano et al. (1998).

For each object detected in the sum of the *BVRI* weighted frames, a radial intensity profile was obtained, sampling the light into elliptical annuli with axes proportional to the object intensity-weighted second-order moments. Following Fasano et al. (1998) we chose to carry out the analysis on a circularly symmetrized profile, where the radial distance along the semimajor axis a_n is $r_n = (a_n/\epsilon^{1/2})$, where ϵ is the Sextractor elongation parameter.

A multi-Gaussian expansion of these symmeterized profiles has been developed as described below. If $I(r)$ is the true, deconvolved profile of the object, it is possible to obtain a simple but effective approximation of it:

$$I(r) = L_T \sum_{j=1}^{M} \frac{b_j}{2\pi s_j^2} \exp\left(-\frac{r^2}{2s_j^2}\right), \quad (1)$$

where L_T is the total luminosity of the source and s_j and b_j are the spread parameter and the weight of each Gaussian, respectively. We adopt $M = 6$ as a compromise between the need of sampling the profile with the maximum allowed number of Gaussians and the need of performing a well-posed fit. Weighting parameters are obviously not independent: their sum must be equal to 1.

In an analogous way an expansion of the normalized point-spread function (PSF) in the frame was carried out, so that it was possible to have an analytical solution of the convolution integral:

$$I_{\rm conv}(r) = L_T \sum_{j=1}^{M} \sum_{i=1}^{N} \frac{a_i b_j}{2\pi(s_j^2 + \sigma_i^2)} \exp\left[-\frac{r^2}{2(s_j^2 + \sigma_i^2)}\right], \quad (2)$$

where the terms with index "i" refer to the multi-Gaussian expansion of the PSF. Once the PSF expansion is known, it is possible to fit equation (2) to the observed points, obtaining the spread and weighting parameters s_j, b_j of the deconvolved profile.

In order to verify the reliability of the deconvolution technique in our particular case, we have performed two checks. First of all we have produced a set of simulations specifically designed to reproduce typical conditions in our sample. Second, we have compared, for a bright galaxy subsample, intrinsic half-light radii derived from the *I*-band galaxy profiles taken at the NTT with that derived from a relatively deep image in the *I* band taken at the WFPC2 on *HST*.

In the first check, intensity profiles have been reproduced as in the observed NTT Deep Field assuming the same pixel sampling and the same average seeing (FWHM $\sim 0\farcs8$). Assuming an intrinsic exponential profile, a series of synthetic images was constructed using different half-light radii ranging from $r_{\rm hl} = 0\farcs1$ to $r_{\rm hl} = 0\farcs9$ with a step of $0\farcs1$. An average of 25 random objects were computed for each radius, assuming a total magnitude of $I \simeq 23.5$ and of $I \simeq 24.7$, which are typical values for a bright and a faint object in our sample. In this way the signal-to-noise ratio is constant in the simulations. In order to reproduce the average seeing conditions in the NDF, the background-subtracted image of a bright star was selected in the field. Its normalized profile was then convolved with the synthetic images of the disk galaxies. The convolved two-dimensional profiles were randomly inserted in regions of the NTT Deep Field far from very bright objects to reproduce with the appropriate pixel size and noise levels the observed NTT galaxies. Finally, the multi-Gaussian deconvolution technique was applied to the synthetic data. We first notice that we have no selection bias against galaxies with large size ($r_{\rm hl} \sim 1$) and low surface brightness down to $I \simeq 24.7$ since all the synthetic objects were detected.

The results are shown in Figure 2, where the error bars represent the dispersion around the mean due to noise in the background subtraction. A good match between the intrinsic and measured half-light radii has been obtained up to $r_{\rm hl} \sim 0\farcs7$. For larger values, a slight underestimate in the measured values appears particularly for the faint subsample. In any case it can be seen that, even for the faint galaxies with $I \sim 25$, the overall correlation between intrinsic and measured half-light radii is preserved in such a way that an intrinsically large, faint object, e.g., with $r_{\rm hl} \sim 0\farcs7$, cannot be detected as a small-sized one, e.g., with $r_{\rm hl} \sim 0\farcs1$. The simulation shows that the fraction of small size galaxies observed in the NDF is real and is not due to intrinsically larger objects which have been shrunk by noise effects.

For the brighter galaxies we had the opportunity to check directly the reliability of our deconvolution technique comparing our *I*-band image photometry of the NTT Deep Field with the *I*-band WFPC2 image photometry taken from the *HST* archive.

We have applied to the WFPC2 galaxies the same deconvolution technique using an average PSF derived from the available stellar profiles in the field. Since the WFPC2 image is not as deep as the NTT *I*-band image and the overlap between the two images is limited to less than half of the field, the comparison was limited to a few relatively bright objects with $I < 24.5$. In Figure 3 the deconvolved half-light radii derived from ground-based and *HST I*-band images are compared. The agreement is very good with a rms difference of 0.05. A similar agreement for the galaxy scale lengths has been found by Schade et al. (1996) for a sample of Canada France Redshift Survey galaxies that are

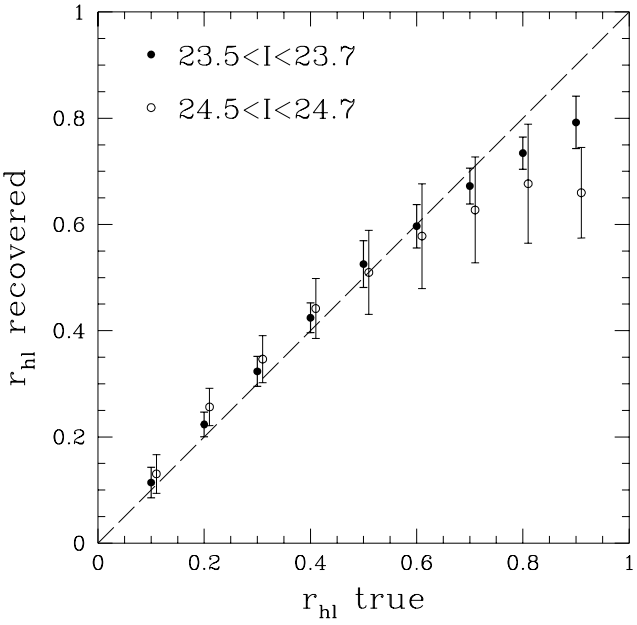

FIG. 2.—Deconvolved half-light radii as a function of true values in simulated data. Filled points are for the bright objects, and empty for the faint ones. Error bars are 1 σ confidence intervals.

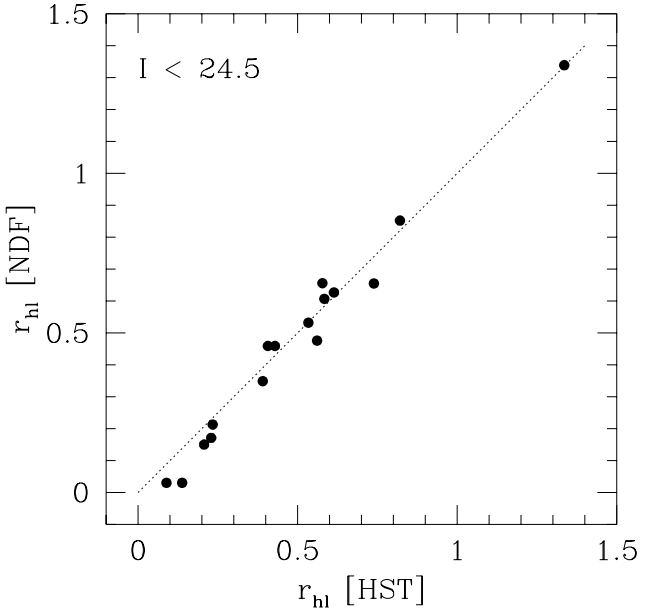

FIG. 3.—Half-light radii obtained deconvolving the *HST* and NDF images of the same objects in the *I* band. The straight line represents equal values.

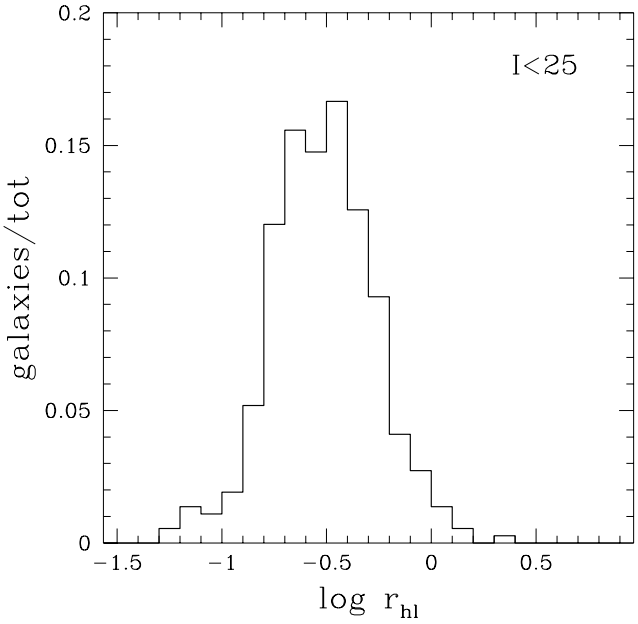

FIG. 4.—Distribution of the half-light radius for galaxies with $I \leq 25$. The values are in log (arcsec).

2 mag brighter, $I_{AB} < 22.5$. Thus, although *HST* images allow more detailed morphological studies with a decomposition of the intensity profiles into more components (e.g., bulge plus disk decomposition), the statistical information is limited by the small field of view. A large amount of statistical information on the galaxy r_{hl} from wide-field ground-based images can be used to constrain the models of galaxy formation. As a first step, we have applied this technique to the multicolor NTT Deep Field. The results are discussed in the next section.

4. THE DISTRIBUTION OF THE GALAXY SIZES IN LUMINOSITY AND REDSHIFT

The distribution of the half-light radii r_{hl} for all the galaxies in the multicolor catalog with $I < 25$ is shown in Figure 4. The median value of the distribution is $r_{hl} \simeq 0''.3$, which confirms previous findings from the *HST* Medium Deep Survey (MDS). In fact, the derived distribution is very similar to that of the MDS (Roche et al. 1998). This is an important result since it has been obtained by means of ground based observations.

Assuming that all the galaxies are characterized by a disk with a given scale length $r_d = r_{hl}/1.68$, we have computed the linear size for each galaxy as a function of redshift using the color estimated redshifts as discussed in § 2. The resulting luminosity-size relation is shown in Figure 5 in two redshift intervals. Uncertainties in the redshift estimates $\Delta z \sim 0.1$ produce uncertainties in the sizes and luminosities $\sim 5\%$ and $\sim 30\%$, respectively.

Figure 5 shows a concentration of faint galaxies with $r_d < 3$ kpc that is present at $M_B > -19$. This is more evident in the $0.4 < z < 0.8$ interval where the galaxy distribution extends down to $M_B \sim -16$.

The histogram of the size distribution is shown in Figure 6 in the same redshift intervals where a peak of low-luminosity dwarf galaxies appears for $r_d \leq 2$ kpc.

However, the assumption of a disklike structure for the majority of the faint galaxies can no longer be valid because of the presence of a noticeable fraction of dwarf galaxies with irregular morphology. Although it is not clear if the images of the high-*z* galaxies seen at progressively shorter wavelengths can produce a spuriously increasing number of

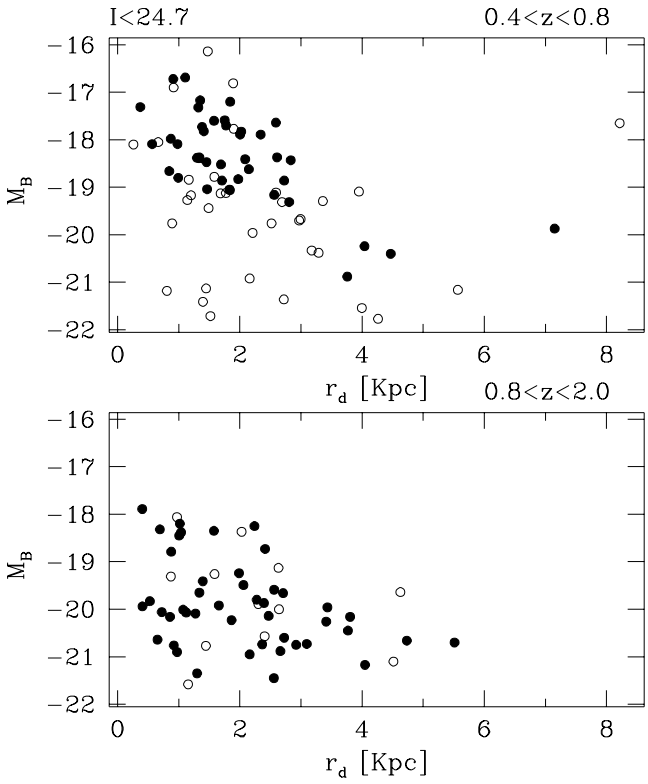

FIG. 5.—Disk scale length ($r_d = r_{hl}/1.68$) as a function of luminosity for galaxies with $I \leq 25$ in two redshift intervals. Filled circles correspond to the disk-dominated subsample whose selection is shown in Fig. 6 and discussed in § 4.

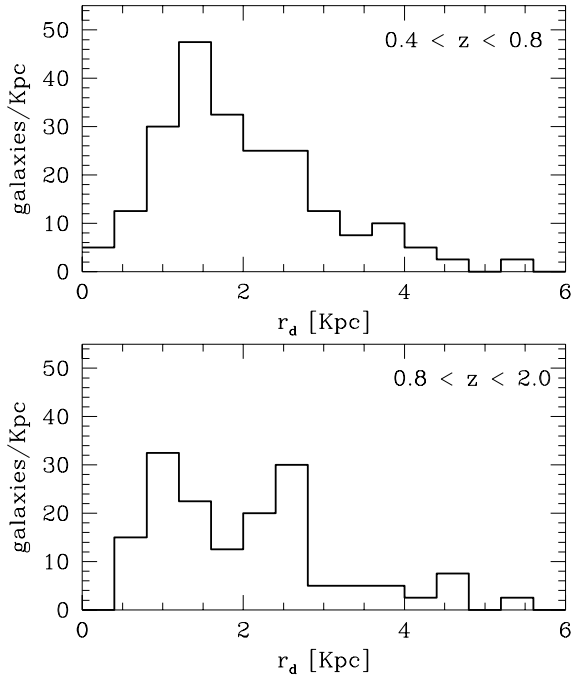

FIG. 6.—Histogram of the differential size distribution for two redshift intervals. The plotted numbers are galaxies per 5 arcmin^2 field per kpc.

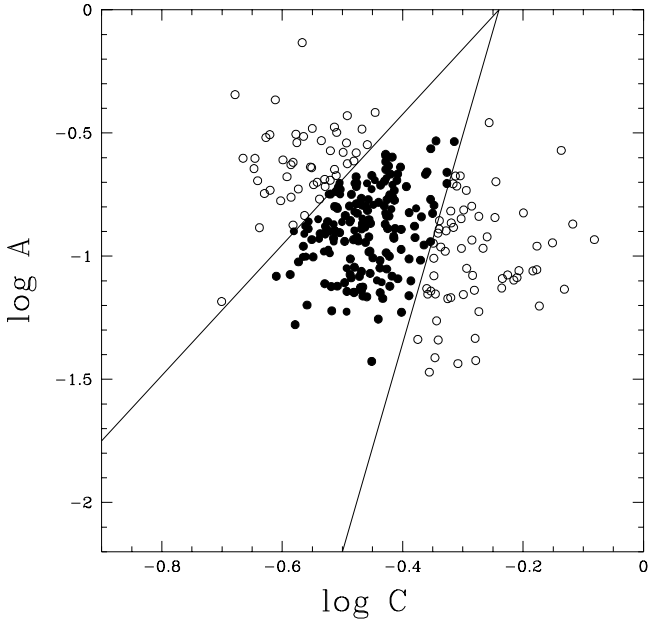

FIG. 7.—Distribution of the galaxies with $I \leq 25$ in the asymmetry-concentration plane (see text). The two straight lines delimit regions corresponding to different spectral types according to Abraham et al. (1996). The region inside the lines is occupied by normal spirals. The outside region toward low concentration and high asymmetry is occupied by galaxies with irregular morphology. Finally, the outside region toward high concentration and lower asymmetry is occupied by S0 and few elliptical galaxies.

irregular galaxies, we have attempted to exclude galaxies with irregular morphology following the method described in Abraham et al. (1996). With this method, galaxies are separated into three classes (irregulars, spirals, and S0 ellipticals) according to the values of their asymmetry and concentration parameters. The asymmetry parameter is defined as

$$A = \frac{1/2 \sum |I_{i,j} - I^{180}_{i,j}|}{\sum I_{i,j}} - k \,, \tag{3}$$

where I and I^{180} are the background-subtracted intensity of the original image and the same after 180° rotation around the baricenter, respectively. Here the sum is extended to the isophotal detection area of every source, and k takes account of the bias introduced in A by the underlying portion of the sky with the same area and shape as the object. For the concentration parameter we have

$$C_\alpha = \frac{\sum_{i,j \epsilon S_\alpha} I_{i,j}}{\sum_{i,j \epsilon S} I_{i,j}} \,, \tag{4}$$

where S refers to a circular aperture with a radius r so that it has the same number of pixels as the isophotal detection area of the object. In an analogous way S_α is an inner circular area with radius $r_\alpha = \alpha r$. We chose to adopt $\alpha = 0.4$ instead of $\alpha = 0.3$ because we found that this larger value takes account of the seeing blurring of the sources in the NDF compared to the *HST* high-resolution images. The distribution in the asymmetry-concentration plane shown in Figure 7 is in good agreement with the Abraham et al. (1996) distribution derived from the Hubble Deep Field galaxies of comparable magnitude.

In Figure 7 regular spiral galaxies are distributed in the central region delimited by the two straight lines defined in Abraham et al. (1996). Their distribution in the luminosity-

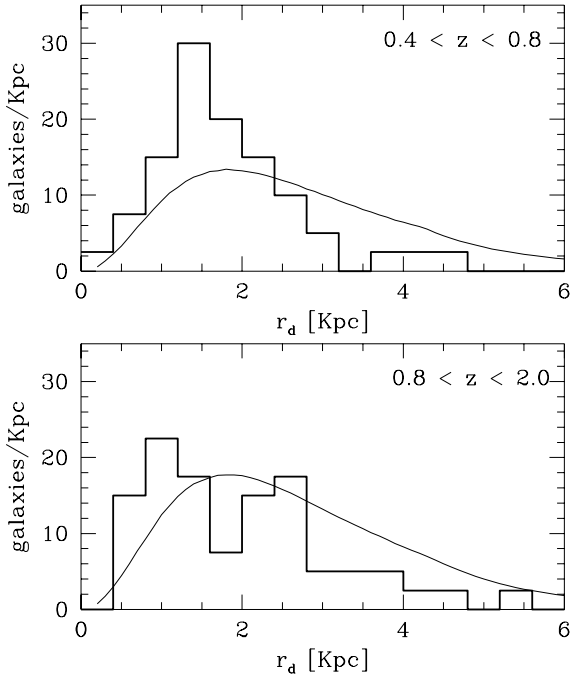

FIG. 8.—Size distribution of galaxies as shown in Fig. 6 but for galaxies having compactness and asymmetry typical of normal spirals. These galaxies are inside the region delimited by the two straight lines in Fig. 7. The continuous curve is the distribution predicted by the CDM model described in § 5. To compare with the observed data in our sample, we have considered in the predicted counts a magnitude limit at $I < 25$. This limit has the effect of selecting brighter (and hence larger) objects at higher z. Such an effect tends to balance the decrease with z of the disk size predicted by CDM models (as shown in Fig. 10 at given absolute magnitude); thus the predicted distributions in the two redshift intervals show an apparent lack of evolution with z.

size plane is also shown by filled symbols in Figure 5. We have reproduced in Figure 8 the size distribution of the normal spirals in the same redshift interval as in Figure 6. It can be seen that even reducing the sample to the more regular spirals, the size distribution in Figure 8 is very similar in shape to that of the whole sample shown in Figure 6 with a peak at very small sizes $r_d \sim 1.5$ kpc. This is expected since the distribution of disk-dominated systems in the luminosity-size plane (filled circles in Fig. 5) follows the distribution of the whole sample.

This behavior has interesting consequences for cosmological scenarios of galaxy formation.

5. EVOLUTION OF GALACTIC DISKS IN CDM COSMOLOGY

The size distribution of different spectral types as a function of redshift is in principle a powerful tool to constrain models of galaxy formation in hierarchical CDM cosmogonies.

Indeed, in these models the galaxy formation proceeds through subsequent merging of small units into larger ones, corresponding to a hierarchical growth of the typical mass of virialized condensations. Since these models predict galaxies in the range $1 < z < 3$ to be still assembling, the corresponding size growth should be detectable by present-day surveys.

Quantitatively, to compare the predictions of the CDM models with deep imaging observations, one needs to express the outcomes of the hierarchical clustering picture in terms of observable properties, i.e., luminosities and sizes. The first goal is usually pursued through the use of semianalytical models (White & Frenk 1991; Cole et al. 1994; Kauffmann et al. 1993; Baugh et al. 1998), which are able to predict luminosity functions and Tully-Fisher relations in reasonable agreement with existing observations. As for the galaxy sizes, quantitative attempts to relate them to the mass growth of cosmic structures have been done only for the regular spiral population (Mo, Mao, & White 1998).

To compare with observations we have to connect the galaxy sizes with their luminous properties. To this aim, we first used the Mo et al. (1998) model to connect the scale length of any exponential disk R_d to the dark matter (herafter DM) circular velocity v_c; then we used the approach of semianalytical models to connect v_c to the luminous properties of galaxies. The predicted relations among luminosity, size, and redshift of the field spirals have then been used to derive statistical distributions which have been compared with the observed ones.

5.1. *Size–Circular Velocity Relation*

In the framework of present theories of galaxy formation, the size of the disk R_d can be related to the circular velocity of the disk (v_d) and of the DM (v_c) halo, assuming that the mass and angular momentum of the baryonic material that settles into the disk are fixed fractions—m_d and j_d—of the DM mass m and angular momentum J (see Mo et al. 1998). The latter can be expressed in dimensionless units $\lambda \equiv J/(|E|^{1/2}/Gm^{5/2})$, whose distribution $p(\lambda)$ is known from several N-body experiments (see Warren et al. 1992; Cole & Lacey 1996; Steinmetz & Bartelmann 1995).

For a galaxy DM density profile of the form given by Navarro, Frenk, & White (1997, hereafter NFW), it is found that

$$R_d = \frac{1}{\sqrt{2}} \left(\frac{j_d}{m_d}\right) \lambda \frac{v_c}{10\ H(z)} f_c(c)^{-1/2} f_R(\lambda, c, m_d, j_d)\ , \quad (5)$$

where $H(z)$ is the Hubble constant at redshift z and $c = r_s/r_{200}$ is the concentration factor expressed in terms of the scale radius r_s in the NFW distribution and of the virial radius r_{200}. The function f_c is related to the total energy of the NFW profile while f_R includes also the gravitational effect of the disk in the density distribution. Fitting formulas for the last two functions are provided by Mo et al. (1998).

Note that in the above model the disk contributes to the rotation velocity, increasing by more than 20% the value of v_c given by the DM halo. We have taken this effect into account in our computations. The power spectrum of the initial DM density perturbation (from which the DM halos are thought to be formed via gravitational instability) enters the computation through the concentration factor c.

According to the above discussion, and following the lines in Mo et al. (1998), we have computed the R_d-v_d and the R_d-v_c relations for different CDM perturbation spectra. In order to compare the results with the outcome of the data analysis we have converted the R_d-v_d (or R_d-v_c) relationships into R_d-M_B as described in the next section.

5.2. *Size-Magnitude Relation Using a Model for Galaxy Formation*

To implement the present understanding of the process of galaxy formation and evolution—and thus to associate magnitudes to the DM galaxy masses—we propose an analytical rendition of the semianalytical approaches introduced by Kauffman et al. (1993) and by Cole et al. (1994) and subsequently developed by several authors (see Somerville & Primack 1998). In these models the DM halos form through the gravitational instability of initial random density fluctuations whose power spectrum depends on the nature of the DM. The baryons within the DM halo, heated to the virial temperature of the halo, are assumed to be distributed in three phases: a cold phase where the gas is radiatively cooled and star formation may occur, a condensed phase (stars), and a hot phase (gas reheated by supernovae explosions). The hierarchical merging of the halos (followed by the possible merging of the galaxies contained in the halos) and the luminosity evolution due to the evolution of the stellar population are also included in the model.

The interplay among these phases and the details of our implementation of the hierarchical models of galaxy formations are given in the Appendix. Following the lines in the literature, the parameters regulating the star formation have been chosen so as to match the local observed properties of the galaxies, i.e., the I-band Tully-Fisher relation and the B-band luminosity function. However, since the disk velocity v_d is $\sim$20% higher than that of the DM, matching the predictions of the model with both the above observables is critical; e.g., setting the star formation parameters to maximize the match to the observed Tully-Fisher relation for a "Milky Way" galaxy with $v_c = 220$ km s^{-1} yields an excess of bright galaxies in the local luminosity function (as noted by Somerville & Primack 1998). A further and complementary constraint is provided by the faint end of the luminosity function; minimizing the mismatch between the observed

and predicted Tully-Fisher relation at faint magnitudes leads to a luminosity function too steep at the faint end.

For these reasons, we have selected the set of free parameters that minimizes the discrepancy of the model results with respect to both the local Tully-Fisher relation and the local B-band luminosity function. For the angular momentum parameters (determining the v_c/v_d ratio and thus affecting the predicted Tully-Fisher relation) we have obtained $j_d = m_d = 0.3$. For the star formation parameters we have obtained the set reported in the Appendix. For the cosmology we have adopted a tilted CDM cosmogony (normalized to *COBE*; with $\Omega_0 = 1$ and $H_0 = 50$ km s^{-1} Mpc^{-1}); the predictions of semianalytical models with such a power spectrum are very close to the mixed (hot + cold) DM models, which are in fair agreement with the data for a wide set of observations (see Primack et al. 1995). With this recipe we have obtained a reasonable agreement of the model prediction with the local luminosity function and Tully-Fisher relation (Fig. 9). The growth of the disk size with cosmic time, a characteristic prediction of CDM models, is shown in Figure 10. The size distributions, plotted at different z for two ranges of absolute magnitudes, are computed convolving equation (5) over the full distribution $p(\lambda)$ of the halo angular momentum λ that a galaxy with given R_d and v_d can have at any z. We have taken for $p(\lambda)$ the expression given in Mo et al. (1998).

5.3. *Results and Comparison with the Observations*

In Figure 11 we show how the galaxy sizes are distributed in absolute magnitude in four redshift intervals. The dots are the observed data, while the shaded regions correspond to the CDM predictions. The latter depend on the value of the dimensionless angular momentum λ, which is distributed according to the function $p(\lambda)$ in the interval $0.025 < \lambda < 0.1$, the extreme values being the 10% and 90% points of $p(\lambda)$, respectively. The solid line corresponds to $\lambda = 0.05$, i.e., to the 50% point of the distribution $p(\lambda)$.

Note that at bright ($M_B < -19$) magnitudes the observed points are approximately equally distributed above and below the solid line and fall in the region allowed by the CDM model. In fact, for the bright galaxies (where a measurement of the disk rotation velocity has been possible) the model by Mo et al. (1998), relating size and circular velocity, is in agreement with the observations; since our model Tully-Fisher relation relating v_d to M_B is also in agreement with observations (see Fig. 9), the matching between our predicted and observed distributions provides a consistency check of the theoretical approach used to derive the galaxy properties in CDM models. However, at fainter magnitudes ($M_B > -19$), the observed sizes tend to occupy systematically the small-sized region below the 50% locus of the angular momentum distribution.

To investigate this point more quantitatively, the differential size distribution of galaxies with $I < 25$ is shown in Figure 8 for different redshift bins. Here the model results include the full $p(\lambda)$ distribution to take account of all the values of angular momentum that a galaxy with given R_d and v_d can have at a given z. To compare the model with the observed data in our sample, we have also introduced a magnitude limit at $I < 25$. This limit has the effect of selecting brighter (and hence larger) objects at higher z. This effect tends to balance the decrease with z of the disk size predicted by CDM models (as shown in Fig. 10 at given absolute magnitude), resulting in an apparent lack of evolution with z of the distributions predicted by the CDM model (see Fig. 8).

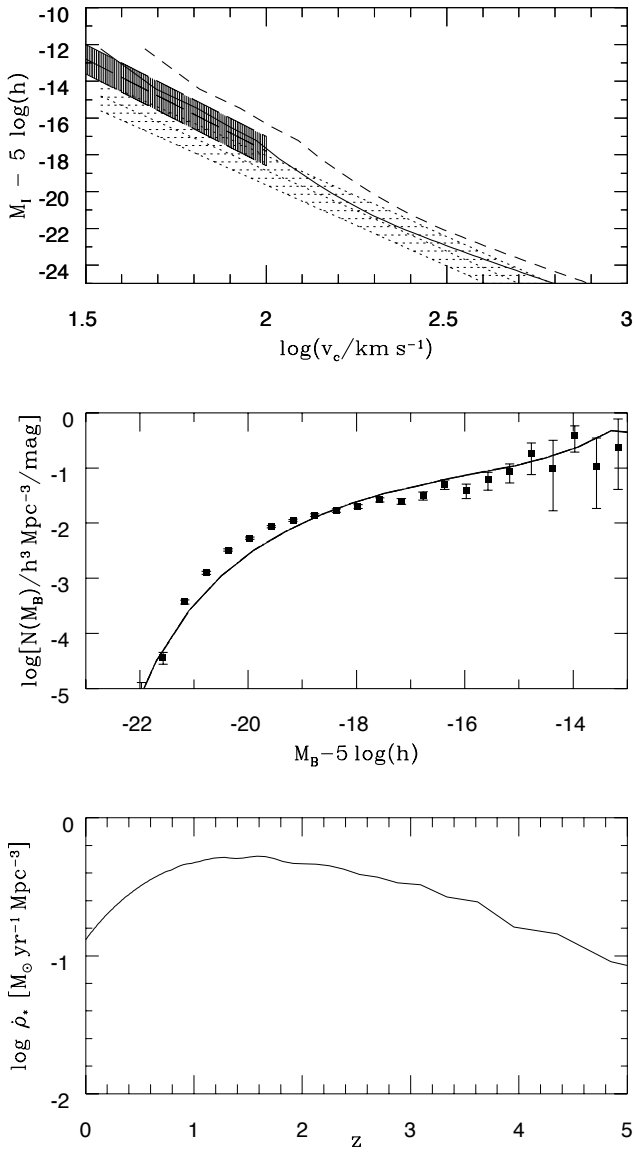

FIG. 9.—*Top*: Tully-Fisher relation; the shaded area represents the region allowed by the observations; the continuous curve is the predicted T-F relation for the dark matter circular velocity, while the dashed curve is the T-F relation for the disk circular velocity. *Middle*: the predicted local luminosity function; the data are adapted from Zucca et al. (1998). *Bottom*: the predicted total star formation rate as a function of redshift.

The comparison with the data shows a general agreement, although an excess of small-sized objects is evident with respect to the CDM predictions. This points toward a galaxy size evolution from high to low z slower than predicted by CDM models, with the persistence of small-sized objects dominating in number at faint magnitudes and at intermediate to low redshifts. The differential distributions in Figure 8 are plotted in terms of absolute numbers in our 5 arcmin^2 field, so that the excess at small sizes over the CDM predictions is not affected by any possible incompleteness at the large/bright end of the distribution, which could be present at lower z in our limited size field.

We also note that the excess is robust with respect to any possible systematic errors in the selection of disk galaxies

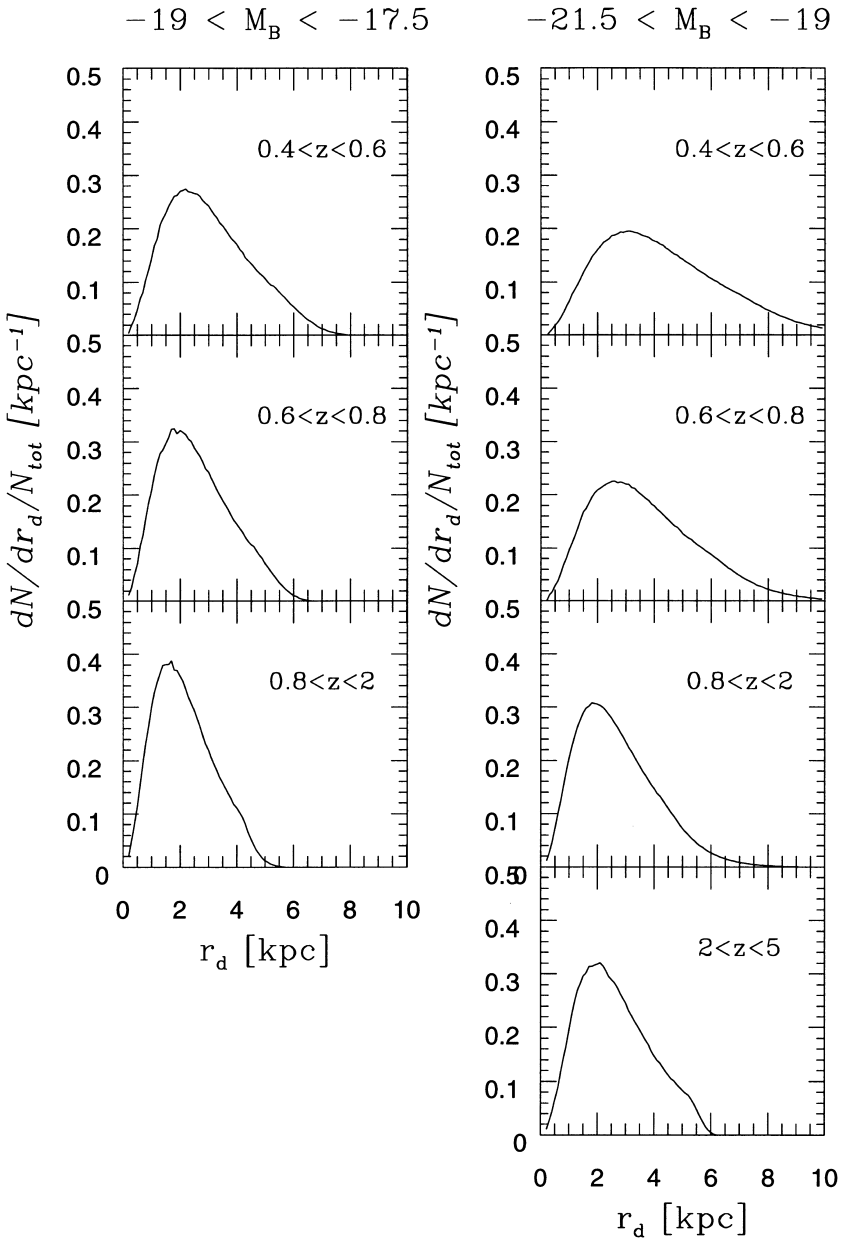

FIG. 10.—Fractional size distribution of galaxies predicted by the CDM model at different z for two ranges of absolute magnitude. The distribution results from the distribution of angular momentum λ, which is related to the disk radius R_d and circular velocity v_d by eq. (5). The dependence on the circular velocity is translated into a dependence on absolute magnitude through the Tully-Fisher relation predicted by the model and shown in the first panel of Fig. 9. Note the growth of the average disk size with cosmic time typical of CDM scenarios.

using the concentration-asymmetry plane shown in Figure 7. Indeed, when the whole sample is considered (including also bulge and irregular systems) the resulting distributions shown in Figure 6 are very similar to the distributions of the "spiral" sample shown in Figure 8. In particular, the excess with respect to the CDM predictions at small sizes is still present.

6. CONCLUSIONS

The size distribution in a ground-based sample of faint galaxies to $I = 25$ is peaked at $r_{hl} \simeq 0''.3$, in good agreement with that found at similar magnitudes in the *HST* MDS.

A morphological selection based on the asymmetry and concentration parameters gives a distribution similar to the one found by Abraham et al. (1996) from *HST* data. From this distribution a sample of normal spirals has been selected. Photometric redshifts have been obtained for this sample using the available multicolor catalog.

A clear distinction in the morphological properties of galaxies fainter or brighter than $M_B \simeq -19$ has been found, especially in the $0.4 < z < 0.8$ redshift interval. In particular the fainter galaxies show a marked concentration toward small ($r_d < 3$ kpc) sizes (see Fig. 5).

The comparison of the observed galaxy sizes with those predicted by hierarchical clustering CDM models at intermediate redshifts ($z \sim 0.5$–1) indicates an excess of faint, small-sized galaxies with respect to the model predictions (see Figs. 6, 8, and 11). A better agreement is found at brighter ($M_B < -19$) magnitudes.

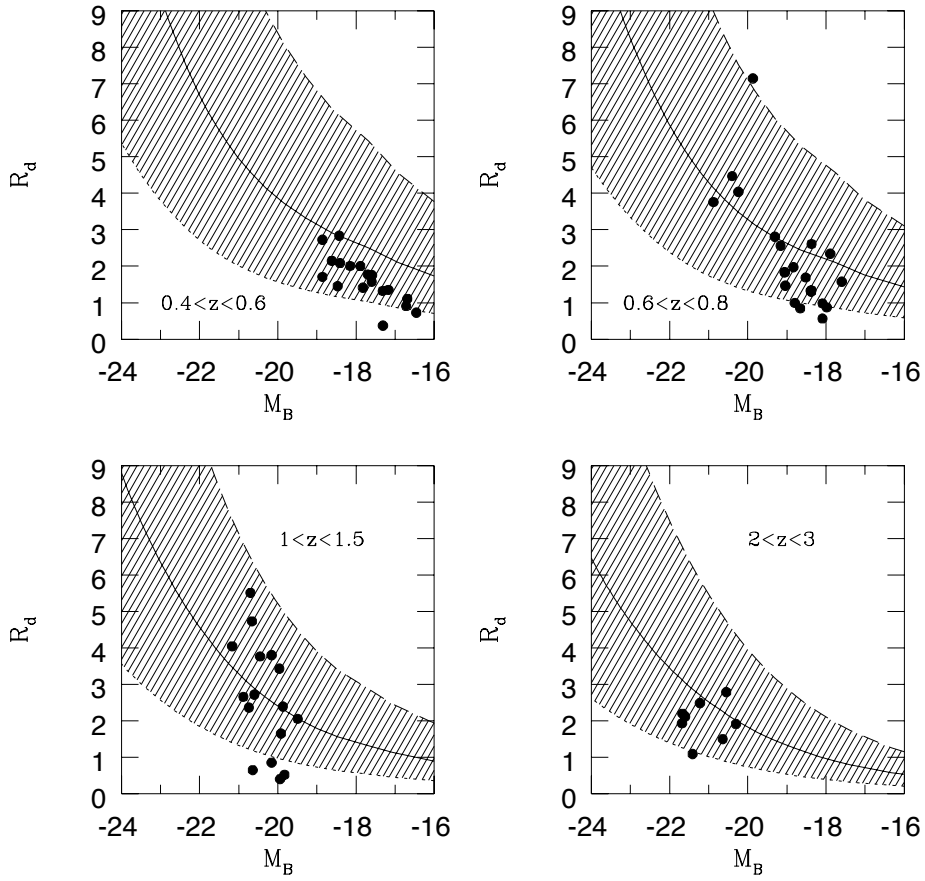

FIG. 11.—Distribution of galaxies in the luminosity-size plane in four redshift intervals. The disk radii are in kiloparsecs. The shaded region represents the region allowed by the model. The upper and lower lines correspond to the 90% and 10% points of the angular momentum distribution. The solid line corresponds to the 50% point of the same distribution (see the text for details).

Different reasons could be responsible for this excess:

1. The ad hoc assumption that all the disks have masses and angular momenta that are a fixed fraction of those of their DM counterparts ($j_d \approx m_d = \text{const.}$) is incorrect for small galaxies. In fact, numerical N-body simulations indicate that the gas loses most of its angular momentum to the DM during galaxy assembly (Navarro & Benz 1991; Navarro & White 1994; Navarro & Steinmetz 1997), although the effect of supernovae feedback (not included in the simulation) is still unclear. In this case, however, the problem of explaining why the assumption $j_d \approx m_d \approx 0.3$ works for more massive galaxies should be solved.

2. The faint end of the galaxy luminosity distribution evolves more slowly than predicted by hierarchical models. The observed population of small galaxies corresponds to the turn-off in the galaxy luminosity function at the faint end, and those galaxies constitute a population evolving in a physically different way from the body of the distribution owing, for example, to the lack of aggregation of objects of small circular velocity. This would break the self-similarity of the hierarchical clustering evolution at small galactic scales.

3. The luminosity of the satellite small galaxies within a given DM halo does not take into account starbursting phenomena due to merging interactions within the halo. For a fixed galaxy luminosity this implies an excess of small size objects.

4. The evolution of the number of galaxies within a halo is poorly described by semianalytical models. The two-body aggregation processes in fact could produce a strong number evolution resulting in an excess of small objects as the redshift increases.

These results have to be checked on a larger sample where the morphological parameters are measured on high-resolution images. The VLT telescopes could be ideal in this respect in terms of field of view, photometric depth, and optical quality. Moreover, a caution should be emphasized when we associate the galaxy morphological properties derived from the observations to the unknown dynamical properties of the faint galaxies. All the previous arguments apply only if these faint objects are sustained by rotation. Rotational curves of galaxies with $I \sim 25$ cannot be measured with the current technology on 8 m class telescopes. Thus, the statistical approach presented in this paper represents a first step to include the galaxy morphology in the CDM models as a new constraint for galaxy formation and evolution.

We thank the referee S. Odewahn for his helpful comments. We are grateful to S. Zaggia for providing *HST* archive images and A. Renzini for discussions. The ultraviolet observations of the NTT Deep Field were performed in SUSI-2 guaranteed time of the Observatory of Rome in the framework of the ESO-Rome Observatory agreement for this instrument.

APPENDIX

THE MODEL OF GALAXY FORMATION

The model proceeds through the following basic steps:

1. We define a time-circular velocity grid, with grid size Δt and Δv_c. Since a given DM halo may contain several galaxies, we denote with V_c the circular velocity of the halos (whose DM mass is M) and with v_c that of the galaxies; the latter represents the depth of the galactic potential wells corresponding to a mass m. The number density $N[V_c, t(z_i)]$ of dark matter (DM) halos with circular velocity V_c present at the initial redshift z_i is taken from the Press & Schechter expression. Initially, we associate to each DM halo a galaxy whose circular velocity v_c is the same of the halo. To each V_c, a halo mass $M = V_c^3/[10GH(z)]$ and a virial temperature T_v are associated. The initial gas content associated to all the halos corresponds to the universal baryonic density Ω_b. The initial stellar content is taken to be 0. For each circular velocity, the baryonic content is divided into a cold gas phase (the one able to cool within the halo survival time τ_l), with mass m_c, into a star phase, with mass m_*, and the complementary hot phase, with mass m_h.

2. For each galaxy circular velocity v_c, we compute the variations of the mass of the gas components and of the stellar content due to merging of DM halos, possibly followed by galaxy merging. At each time step, we first compute (*a*) the probability $P(V'_c, V_c, t)$ that a halo at time t with velocity V'_c is included in a halo with velocity V_c at time $t + \Delta t$, and (*b*) the associated halo merging rate $\partial P(V_c), t \mid V_c)/\partial V_c\, \partial t$: these are computed in the framework of the so-called Extended Press & Schechter Theory (EPST—see Bond et al. 1991; White & Frenk 1991; Bower 1991; Lacey & Cole 1993). Then we compute the number of galaxies $N_g(v_c, V_c, t)$ with circular velocity v_c in a halo with velocity V_c, implementing the canonical recipes of semianalytical models. According to these, during halo merging, a galaxy contained in one of the parent halos contributes to enrich the dominant galaxy of the common halo (of velocity V_c) if its coalescence time $\tau_m(v_c)$ is less than the halo survival time $\tau_l(V_c)$ (predicted in the EPST). In the remaining case ($\tau_m > \tau_l$) the galaxy retains its identity. Thus, for galaxies with $v_c = V_c$, the positive increment in the number of galaxies of given v_c in halos with V_c is linked to the number increment of DM halos with V_c [whose contribution from progenitors V'_c is $N(V'_c, t)\, \partial^2 P(V'_c, t \mid V_c)/\partial V'_c\, \partial t$] through the probability prob $[\tau_m(v'_c) < \tau_l(V_c)]$ of forming one dominant galaxy merging those contained in the parent halos; for galaxies with $v_c \neq V_c$ the positive increment is linked to the complementary probability $1 -$ prob $[\tau_m(v'_c) < \tau_l(V_c)]$. The overall negative increment is due to disappearance of satellite galaxies of velocity v_c in halos V_c, when the latter merge to form larger halos V'_c. Thus

$$
\begin{aligned}
{}_*N_g(v_c, V_c, t + \Delta t) = {} & N_g(v_c, V_c, t) \\
& + \Delta t\, \delta(v_c, V_c) \int_0^{v_c} dv'_c \int_{v_{c'}}^{V_c} dV'_c\, N(V'_c, t)\, \frac{\partial P(V'_c, t \mid V_c)}{\partial V'_c\, \partial t}\, \frac{N_g(v'_c, V'_c)}{N_{gT}(V'_c)}\, \text{prob}\, [\tau_m(v'_c) < \tau_l(V_c)] \\
& + \Delta t \int_{v_c}^{V_c} dV'_c\, N(V'_c, t)\, \frac{\partial P(V'_c, t \mid V_c)}{\partial V'_c\, \partial t}\, \frac{N_g(v_c, V'_c)}{N_{gT}(V'_c)}\, \{1 - \text{prob}\, [\tau_m(v'_c) < \tau_l(V_c)]\} \\
& - \Delta t \int_{V_c}^{\infty} dV'_c\, \frac{\partial P(V_c, t \mid V'_c)}{\partial V_c\, \partial t}\, N_g(v_c, V_c)\,, \qquad \text{(A1)}
\end{aligned}
$$

where $\delta(v_c, V_c) = 1$ for $v_c = V_c$ and 0 elsewhere.

Here $N_{gT}(V_c) = \int dv'_c\, N_g(v'_c, V_c, t)$ is the total number of galaxies in the halo V'_c. The merging time of the galaxies is parameterized [in terms of the DM masses $M(V_c)$ and $M'(V'_c)$] as $\tau_m = \tau_0(M'/M)^{\alpha_{\text{merg}}}$ according to Cole et al. (1994), while the probability prob $[\tau_m(v'_c) < \tau_l(V_c)]$ for a DM halo of velocity V_c to have a survival time τ_l larger than a given value has been computed by Lacey & Cole (1993) (see their eq. [2.21]) in the framework of the EPST. The initial condition is such that in each halo there is only one galaxy [i.e., $N_g(v_c, V_c, t_0) = N(V_c, t_0)$ for $v_c = V_c$ and 0 elsewhere]. From the ratio $N_g(v_c, V_c, t)/N(V_c, t)$ we compute the probability $f(v_c, V_c, t)$ of finding a galaxy with circular velocities v_c in a DM halo of circular velocity V_c. Then the total number density of galaxies with circular velocity v_c [and the corresponding probability density $p(v_c, t)$] is computed from $N_g(v_c, t) = \int_{v_c}^{\infty} dV_c\, N(V_c, t) f(v_c, V_c, t)$, where the halo distribution $N(V_c, t)$ takes the canonical Press & Schechter form.

Finally, for each v_c we compute the probability distribution $p(v'_c, v_c, t)$ of having a galaxy at time t with circular velocity v'_c included in a galaxy with circular velocity v_c at time $t + \Delta t$. This is given by $p(v'_c, v_c, t) = \int_{v_{c'}}^{\infty} \int_{v_c}^{\infty} dV_c\, dV'_c\, P(V'_c, V_c, t) f(v'_c, V'_c, t) f(v_c, V_c, t)$; from this we also derive the associated conditional probability $p(v'_c, t \mid v_c) = p(v'_c, t \mid v_c)/p(v_c, t)$ that, *given* a galaxy with velocity v_c at time t, a galaxy v'_c has been included in it at $t - \Delta t$.

The average increments of the cold gas mass and the stellar mass in galaxies with circular velocity v_c are given by the equations in White & Frenk (1991); in differential form these read

$$
m_c(v_c, t + \Delta t) = m_c(v_c, t) + \Delta t \int_0^{v_c} dv'_c\, \frac{N_g(v'_c, t)}{N_g(v_c, t)}\, p(v'_c, t \mid v_c)\, m_c(v'_c, t) \qquad \text{(A2)}
$$

$$
m_*(v_c, t + \Delta t) = m_*(v_c, t) + \Delta t \int_0^{v_c} dv'_c\, \frac{N_g(v'_c, t)}{N_g(v_c, t)}\, p(v'_c, t \mid v_c)\, m_*(v'_c, t)\,. \qquad \text{(A3)}
$$

The hot gas reservoirs are assumed to be retained in the DM halos rather than in individual galaxies. The amount of hot gas in halos with velocity V_c is given by

$$m_h(V_c, t + \Delta t) = m_*(V_c, t) + \Delta t \int_0^{V_c} dV'_c \frac{N(V'_c, t)}{N(V_c, t)} \frac{\partial P(V'_c, t \mid V_c)}{\partial V'_c \, \partial t} m_h(V'_c, t) \quad . \tag{A4}$$

3. The mass of the cold phase is further incremented by the cooling: the gas that cools in a halo with V_c in the time step Δt is $\Delta m_c(V_c) = 4\pi r_{\rm cool}^2 \rho_g(r_{\rm cool}) \Delta r_{\rm cool}$, where ρ_g is the gas density and the dependencies of the cooling radius $r_{\rm cool}$ on V_c and t are given, e.g., in Somerville & Primack (1998). Such cooled gas is assigned to the galaxies that have the same circular velocities of their DM halo, so that the average hot gas in galaxies with circular velocity v_c is $\Delta m_c(v_c) = \Delta m_c(V_c)\ N_g(V_c, V_c)/\int dV'_c\ N_g(V_c, V'_c)$.

The amount of cold gas that forms stars is then computed and the corresponding mass is transferred from the cold phase to the star phase. This amount is $\Delta m_*(v_c, t) = \dot{M}_* \Delta t$, and it is regulated by the star formation rate $\dot{m}_*(v_c, t) = [m_c(v_c, t) - m_*(v_c, t) - m_h(v_c, t)]/\tau_*$, which is as in Cole et al. (1994). The timescale $\tau_*(v_c) = \tau_*^0 (v_c/300 \text{ km s}^{-1})^{\alpha_*}$ is parameterized according to Cole et al. (1994).

A final transfer from the cold phase back to the hot phase, owing to supernova feedback, involves the amount $\Delta m_h(v_c, t) = \beta(v_c)\Delta m_*(v_c, t)$ where $\beta = (v_c/v_h)^{\alpha_h}$ is defined by the free parameters v_h and α_h. The total hot gas returned to a halo with velocity V_c by the member galaxies is $\Delta m_h(V_c) = \int_0^{V_c} dv_c\, N_g(v_c, V_c, t)\Delta m_h(v_c, t)$.

4. For each circular velocity v_c, the associated luminosity at wavelength λ is computed by the convolution

$$S_\lambda = (1/\Gamma) \int_0^t \phi_\lambda(t - t') m_*(t') dt' \ , \tag{A5}$$

where the spectral energy distribution of luminous stars $\phi_\lambda(t)$ is taken from the stellar population synthesis models by Bruzual & Charlot (1996). The output normalization depends on the free parameter Γ, i.e., the fraction of "stellar" mass locked in nonluminous objects (planet-like objects). The dust absorption is included in the computation with the same procedure described in Somerville & Primack (1998).

5. We increment the current time by Δt and repeat the whole procedure from step (2) until the output time is reached.

As explained in the text, we choose our parameters in order to fit both the local observed Tully-Fisher relation and the local observed B-band luminosity function. For the star formation parameters, the above procedure yields the following set:

$\tau_*^0 = 2$ Gyr, $\alpha_* = -0.5$, $v_h = 100$ km s^{-1}, and $\alpha_h = 5$ for the stellar formation.

$\Gamma = 1$ and $\Omega_b = 0.06$ for the normalization of the mass-to-luminosity ratio.

$\tau_0 = 0.1$ dynamical times, and $\alpha_m = 0.2$ for the galaxy merging rate. In addition, a cutoff in the cooling for halos with $v_c > 500$ km s^{-1} is included (see Somerville & Primack 1998).

REFERENCES

Abraham, R. G., Tanvir, N. R., Santiago, B., Ellis, R. S., Glazebrook, K., & van den Bergh, S. 1996, MNRAS, 279, L47
Arnouts, S., D'Odorico, S., Cristiani, S., Zaggia, S., Fontana, A., & Giallongo, E. 1999, A&A, 341, 641
Baugh, C. M., Cole, S., Frenk, C. S., & Lacey, C. G. 1998, ApJ, 498, 504
Bendinelli, O. 1991, ApJ, 366, 599
Bertin, E., & Arnouts, S. 1996, A&AS, 117, 393
Bond, J. R., Cole, S., Efstathiou, G., & Kaiser, N. 1991, ApJ, 379, 440
Bouwens, R., Broadhurst, T. J., & Silk, J. 1997, ApJ, 506, 579
Bower, R. 1991, MNRAS, 248, 332
Brinchmann, J., et al. 1998, ApJ, 499, 112
Bruzual A., G., & Charlot, S. 1993, ApJ, 405, 536
Cole, S., Aragon-Salamanca, A., Frenk, C. S., Navarro, J. F., & Zepf, S. E. 1994, MNRAS, 271, 781
Cole, S., & Lacey, C. G. 1996, MNRAS, 281, 1176
Connolly, A. J., Szalay, A. S., Dickinson, M., Subbarao, M. U., & Brunner, R. J. 1997, ApJ, 486, L11
Cowie, L. L., Songaila, A., Hu, E., & Cohen, J. G. 1996, AJ, 112, 839
Driver, S. P., et al. 1998, ApJ, 496, 93
Ellis, R. S., Colless, M., Broadhurst, T. J., Heyl, J. S., & Glazebrook, K. 1996, MNRAS, 280, 235
Fasano, G., Cristiani, S., Arnouts, S., & Filippi, M. 1998, AJ, 115, 1400
Fontana, A., et al. 1999, AJ, submitted
Giallongo, E., D'Odorico, S., Fontana, A., Cristiani, S., Egami, E., Hu, E., & McMahon, R. G. 1998, AJ, 115, 2169
Glazebrook, K., Abraham, R., Santiago, B., Ellis, R., & Griffiths, R. 1998, MNRAS, 297, 885
Kauffmann, G., White, S. D. M., & Guiderdoni, B. 1993, MNRAS, 264, 201
Lacey, C., & Cole, S. 1993, MNRAS, 262, 627
Lilly, S. J., Tresse, L., Hammer, F., Crampton, D., & Le Fèvre, O. 1995, ApJ, 455, 108
Lilly, S. J., et al. 1998, ApJ, 500, 75
Madau, P., Ferguson, H. C. L., Dickinson, M., Giavalisco, M., Steidel, C. C., & Fruchter, A. 1996, MNRAS, 283, 1380
Mo, H. J., Mao, S., & White, S. D. M. 1998, MNRAS, 295, 319
Navarro, J. F., & Benz, W. 1991, ApJ, 380, 320
Navarro, J. F., Frenk, C. S., & White, S. D. M. 1997, ApJ, 490, 493
Navarro, J. F., & Steinmetz, M. 1997, ApJ, 478, 13
Navarro, J. F., & White, S. D. M. 1997, MNRAS, 267, 401
Odewahn, S. C., et al. 1996, ApJ, 476, L13
Pascarelle, S. M., Lanzetta, K. M., & Fernandez-Soto, A. 1998, preprint (astro-ph/9809295)
Primack, J. R., Holtzman, J., Klypin, A., & Caldwell, D. O. 1995, Phys. Rev. Lett., 74, 2160
Roche, N., Ratnatunga, K., Griffiths, R. E., Im, M., & Naim, A. 1998, MNRAS, 293, 157
Schade, D., Lilly, S. J., Crampton, D., Hammer, F., Le Fèvre, O., & Tresse, L. 1995, ApJ, 451, L1
Schade, D., Lilly, S. J., Le Fèvre, O., Hammer, F., & Crampton, D. 1996, ApJ, 464, 79
Somerville, R., & Primack, J. R. 1998, preprint (astro-ph/9802268)
Steidel, C. C., Adelberger, K. L., Giavalisco, M., Dickinson, M., & Pettini, M. 1999, ApJ, 519, 1
Steinmetz, M., & Bartelmann, M. 1995, MNRAS, 272, 570
Warren, M. S., Quinn, P. J., Salomon, J. K., & Zurek, W. H. 1992, ApJ, 399, 405
White, S. D. M., & Frenk, C. S. 1991, ApJ, 379, 52
Williams, R. E., et al. 1996, AJ, 112, 1335
Zucca, E., et al. 1997, A&A, 326, 477